Atmos. Meas. Tech. Discuss., 6, 11011–11054, 2013
www.atmos-meas-tech-discuss.net/6/11011/2013/
doi:10.5194/amtd-6-11011-2013

Atmospheric Measurement Techniques Discussions

Aerosol optical properties during dust and biomass burning episodes retrieved from sun-photometer over Shanghai

C. Shi[1], S. Wang[1,3], R. Zhou[1], D. Li[2], H. Zhao[1], R. Liu[1], Z. Li[2], and B. Zhou[1]

[1]Shanghai Key Laboratory of Atmospheric Particle Pollution and Prevention (LAP[3]), Department of Environmental Science and Engineering, Fudan University, Shanghai 200433, China
[2]State Environmental Protection Key laboratory of Satellites Remote Sensing, Institute of Remote Sensing and Digital Earth of Chinese Academy of Sciences, Beijing 100049, China
[3]School of Environment and Architecture, University of Shanghai for Science and Technology, Shanghai 200093, China

Received: 10 November 2013 – Accepted: 2 December 2013 – Published: 17 December 2013

Correspondence to: B. Zhou (binzhou@fudan.edu.cn)

Published by Copernicus Publications on behalf of the European Geosciences Union.

Abstract

Ground-based observation over Shanghai was carried out from 28 March to 25 June 2013 in an urban site at Fudan University (31°18′ N, 121°29′ E). Utilizing a sun/sky radiometer (CE318), aerosol properties including thickness, scattering, asymmetry, and particle size distribution were inversed for two types (dust and biomass burning). Dust aerosol showed large optical depth (AOD at 440 nm ~ 1.06) with small value of Ångström parameter (α) around 0.74, indicating the strong optical extinction capability of large-size particles. Aerosol loading (~ 0.72 at 440 nm) was discovered to be coupled with large α (> 1.05) for biomass smoke. The particle size distribution was dominated by the coarse mode for dust with high concentration ratio between coarse and fine mode (V_C/V_F ~ 3.76). Biomass burning particle primarily accumulated around 0.17 µm and performed smaller V_C/V_F (~ 0.99). Aerosol in fine mode mainly accounted for the optical extinction process in Shanghai as its volume concentration was well-correlated with AOD (R ~ 0.88 in average condition). The value of single scattering albedo (SSA) during agricultural residue burning displayed variation from 0.902 to 0.922 with a descending trend at 670–1020 nm while SSA increased at all wavelengths for dust aerosol. The negative correlation between SSA · AOD and α was analyzed to capture the order of scattering capability: urban/industrial < biomass < dust aerosol. Higher value of asymmetry factor at 1020 nm (~ 0.652) of dust aerosol was found compared to average condition and biomass smoke (both were equaled to 0.625), imposing the enhanced forward scattering of dust particles in NIR band. The validation of AOD vs. MODIS showed errors in dust and biomass samples, which may be attributed to the variable SSA in YRD. The ascending deviation also existed in clear condition, which could be caused by the overestimation of ground reflectance in MODIS algorithm.

AMTD
6, 11011–11054, 2013

1 Introduction

More than 30 yr witnessed the rapid economic growth in China with prosperous industrialization and urbanization, generating various anthropogenic emissions and consequently deteriorating the air quality (Lei et al., 2011; Lu et al., 2011; Westerdahl et al., 2009), descending the air visibility (Jinhuan and Liquan, 2000; Zhang et al., 2011) while increasing aerosol loadings (He et al., 2012a; Xue et al., 2011). Aerosol impacts considerably and plays the key role in global climate change by affecting the radiation energy budget with corresponding uncertainty (Badarinath et al., 2007; Metz et al., 2007; Quaas et al., 2008). Indirectly, aerosol can also participate in the formation process of clouds as condensation nuclei, exerting influences on cloud cover and precipitation distribution (Ramanathan et al., 2001). The optical properties of aerosol serve as a major factor affecting radiative forcing in the performance of scattering and absorption process (Haywood and Boucher, 2000; Jacobson, 2001; Takemura et al., 2002). Studies on climate changes were conducted intensively using aerosol models with parameterized indices including single scattering albedo (SSA) and asymmetry factor (ASY) in numerical simulation (Mugnai and Wiscombe, 1986; Russell et al., 1999; Takemura et al., 2002). Among these radiatively important parameters, SSA was indispensible in estimating ground albedo in remote sensing retrievals while the biggest challenge existed in distinguishing aerosol types (Chu et al., 2003; Kaufman et al., 2001). Aerosols from different sources can be classified into distinctive types with dynamic variations in optical characteristics (Dubovik et al., 2002; Eck et al., 2005). For these aerosols with diverse types, the chemical composition along with hygroscopic growth capability were discovered to be main factors determining optical properties (Eck et al., 2005; Kim et al., 2006). Continental aerosol was found to be mainly constituted with mineral dust, carbonaceous particles from biomass burnings (including agriculture residue and forest fire) as well as marine particles and secondary aerosol (Badarinath et al., 2011; Limbeck et al., 2003; Tsunogai et al., 1985). Due to the microphysical properties of

AMTD
6, 11011–11054, 2013

aerosol present temporal and spatial variability, it is essential to do specific observation on respective aerosol type in different regions (Dubovik et al., 2002).

Yangtze River Delta (YRD) is located in the East China with fast economic development in recent decades, during which aerosol loading was lifted up acutely (He et al., 2012a). As the most populated city cluster in China (with the population more than 150 million till the year of 2011), mixed types of aerosols such as industrial/urban, dust, sea salt and smoke particles were discovered in the boundary layer by abundant studies (Fu et al., 2008; Gao et al., 2009; He et al., 2010; Huang et al., 2011). The Chinese Sun Hazemeter Network (CSHNET) operated a nationwide observation finding that the aerosol optical properties in Eastern China behaved as mixtures of mineral particles, smoke and anthropogenic pollutant (Xin et al., 2005). Distinctive from the aerosol characteristics in northern China, whose seasonal variations were obvious, airborne aerosol loading exhibited daily fluctuations dynamically in contrast to the dimming seasonal changes in YRD (Wang et al., 2006). Investigated and inversed with sun-photometer by Xia et al. (2007), the notable aerosol direct radiative forcing (annually mean surface shortwave radiation and photosynthetically active radiation were computed as $-38.4\,\mathrm{W\,m^{-2}}$ and $-17.8\,\mathrm{W\,m^{-2}}$ respectively) by burdened aerosol loadings was calculated out in Taihu area. Shanghai, the biggest megacity in China, is suited in eastern YRD district and facing East China Sea. The coastal location makes the chemical composition and formation mechanism of aerosol here quite complicated, where sulfate, ammonium, black carbon (BC), mineral and marine can be measured (Li et al., 2010; Wang et al., 2000; Wang et al., 2006; Yang et al., 2009; Ye et al., 2003). So it is of considerable challenge to observe aerosol of single type in this metropolitan (Wang et al., 2009). According to relevant meteorology records of Shanghai, dust storms always invade in Spring through long-range transport and biomass burnings occur in June, July and August after summer harvest. During the air pollution episodes caused by mineral dust and biomass smoke, these two types of aerosols could be predominant pollutants in the ambient air, offering us an unprecedented opportunity to study their microphysical and chemical properties (Fan et al., 2010; Fu et al., 2010;

AMTD
6, 11011–11054, 2013

Wang et al., 2012a; Wang et al., 2009). Researches have adequately indicated the significance of both dust and crop residue burning aerosol in radiation process and climate responses (Shindell and Faluvegi, 2009; Takemura et al., 2005). China Aerosol Remote Sensing Network (CASNET) conducted an overall observation in YRD including two sites in Shanghai, revealing the different contribution of marine and inland aerosols in this coastal city (Pan et al., 2010). Apart from that, urban/industrial aerosol, which mainly consist of insoluble, soluble and soot species, is of broad existence in observation (Hess et al., 1998). Urban aerosols optical properties change with temperature, humidity, solar radiation intensity, altitude, wind speed and displays inhomogeneous distribution in different regions worldwide (Eck et al., 1999). Applying sun photometer with SKYRAD algorithm for retrievals, He et al. (2012b) presented the seasonal variations of optical properties in Shanghai. Their studies demonstrated the very effect of dust and biomass smoke aerosol on optical and radiative characteristics but they were absent from doing a respective analysis on aerosols of different types. Even if a certain type of aerosol is in dominance at one location, variability still behaves dynamically thanks to the meteorological conditions (Dubovik et al., 2002; Kim et al., 2004).

Using the observational data from 28 March to 25 June in 2013, this study aims to perform a comparative investigation on aerosol optical properties during spring dust and summer biomass burning episodes over Shanghai. Aerosol optical parameters (including optical depth, size distribution, volume concentration, single scattering albedo and asymmetry factors) were inversed by the optimized algorithm based on the classic one introduced by Dubovik and King (2000). Comparisons between the characteristics of these two types aerosols can serve to better understanding the regional aerosol microphysical and radiative features. The comprehensive learning about the respective type of aerosol should also be an indicator of building precise aerosol models and making revisions for the retrieval scheme. Finally, validations of MODIS AOD products with our ground-based observation results were presented to further discuss the inversion error and optimize the retrieval algorithm.

AMTD
6, 11011–11054, 2013

2 Measurement and methodology

2.1 Observation site and instruments

All in situ measurements of aerosol optical properties and meteorology factors were installed at an urban site (31°18′ N, 121°29′ E) in Shanghai of China from 28 March 2013 to 25 June 2013. Our site is located on the roof of No.4 teaching building about 20 m above ground level in the campus of Fudan University (FDU). As the location along with climatological elements are the primary factors determining aerosol type and its characteristics (Kim et al., 2004), we described the geographical condition in Fig. 1. Shanghai is seated in East China, surrounded by the dense city clusters of YRD and adjacent to Northwest Pacific Ocean. Cold air masses from the north while moist, warm air from the south mix above in spring (March, April and May) and early summer (June). During this period, air-pollution episodes are frequently caused by the dust from the Kumutage/Taklimakan and Mongolian deserts through long-transport (Sun et al., 2001). Biomass burnings always come into one of pollution sources in agricultural harvest season (May and June) in YRD (Fan et al., 2010). It facilitates a considerable contributor of mixed aerosol types with high RH (relative humidity), which accelerates the hygroscopic growth process of smoke particles (Mochida et al., 2006).

The Cimel CE-318N sun/sky photometer applied in this study produced aerosol optical parameters (through inversions) including aerosol optical depth, single scattering albedo, asymmetry factor and size distribution. The automatic tracking sun and sky scanning radiometers made direct sun radiance with a 1.2° field of view in an interval of 15 min in the eight spectral channels from ultraviolet (UV) to near infrared (NIR) band at 340, 380, 440, 500, 675, 870, 1020 and 1640 nm. The output digital numbers (DN) transformed from direct sun irradiance and diffuse-sky radiance were then transmitted to computer terminal by ASTPWin software and stored as k7 format files. The software can also be used to retrieve aerosol optical depth according to Beer-Lambert law at observed channel (Che et al., 2009). The constant observation of meteorology information was captured by CAMS620-HM (production of

AMTD
6, 11011–11054, 2013

Huatron Environment Technology Co., Ltd) automatic weather station, just 5 m away from sun-photometer. The data of AQI (Air Quality Index) and mass concentration of PM_{10}, $PM_{2.5}$, CO were all downloaded from Shanghai Environmental Monitoring Center (SEMC) website (http://www.semc.com.cn). AOD at 550 nm was also derived from MODIS (MODerate resolution Image Spectrometer) onboard Terra launched by NASA (http://ladsweb.nascom.nasa.gov). We choose the Collection 051 products to make validations with results from ground-based measurement.

2.2 Inversion algorithm and data description

The aerosol inversion algorithm put forward by Dubovik et al. (2000) and developed afterwards (Dubovik et al., 2002, 2006; Holben et al., 2006) was widely applied in AERONET (AErosol RObotic NETwork) established by NASA. Based on the code of this algorithm, two parts were optimized in this study, which differed itself from AERONET operational algorithm. One improvement for the classic algorithm was that a gain-corrected solid angle was introduced to produce interconverting calibrations coefficients during direct solar irradiance and diffuse-sky radiance measurement (Li et al., 2008). The core of radiance calibration transfer was to realize the refreshment of calibration coefficients on basis of radiometric characteristics of CE318. This alternative calibration method has been applied in CARSNET sky measurement in some observation sites (Che et al., 2009). The algorithm takes advantage of the direct-sun irradiance $E(\lambda)$ and diffused-sky radiance $L(\lambda)$ and defines a parameter Ω_v as their ratio:

$$\Omega_v = \frac{E(\lambda)}{L(\lambda)} = \frac{C_s(\lambda)V_s(\lambda)}{C_a(\lambda)V_a(\lambda)} \quad (1)$$

where $C(\lambda)$ and $V(\lambda)$ denote the calibration coefficients and the output DN of CE318 while the subscript s and a are short for sun irradiance and aureole sky radiance. Then the gain-corrected solid angle Ω, which is independent of wavelength, is needed

AMTD
6, 11011–11054, 2013

instead of Ω_v in the calibration transfer:

$$\Omega = \Omega_v(HG_a/LG) \quad (2)$$

where HG_a and LG are the fixed instrument internal electronic gains (this means the gains only depend on instrument). The calibration transfer performs a comparable accuracy using Ω with laboratory calibration coefficients (e.g. 3–5 %). It's well-used to calibrate sky radiance from sun irradiance and could serve to recalibrate the historical measurements.

One of the largest error sources in retrieval is often related with ground reflectance. Li et al. (2006) used the 72 month averaged ground albedo (error ~ 10 %) derived from MODIS to revise the reflectance parameter of the surface, which was also carried out in our retrieval. Additionally, the triplet direct-sun irradiance and almucantar measurement which is similar with AERONET serve to cloud-screening for all parameters. Then we introduce the radiatively important parameters in this study respectively.

AOD can be directly computed through the solar irradiance with Beer-Lambert law reproduced in Eq. (3), where τ is equal to the total scattering and absorption effects (k_{ex} as the extinction coefficient) in the atmosphere column. And the Ångström exponent (α) is calculated from 440 nm and 870 nm (nominal) wavelength in the Eq. (4), where β is the AOD at 1 µm (Ångström, 1964).

$$\tau = \int_0^l k_{ext} \mathrm{d}l \quad (3)$$

$$\tau(\lambda) = \beta\lambda^{-\alpha} \quad (4)$$

The single scattering albedo is defined as the ratio between scattering coefficient (k_{scat}) with total extinction coefficient (k_{ext}, sum of scattering and absorption). It can be calculated by establishing a relationship between the actual and the estimated radiation

AMTD
6, 11011–11054, 2013

parameters after cloud screening and quality control (Li et al., 2004).

$$\omega = \frac{k_{\text{scat}}}{k_{\text{ext}}} = \frac{k_{\text{scat}}}{k_{\text{scat}} + k_{\text{abs}}} \tag{5}$$

Phase functions $p(\Theta)$ are derived from total sky radiance and give rise to size distribution, refractive index, single scattering albedo (ω) of aerosol.

$$2\omega = \int_0^{\pi} \omega p(\Theta) \sin(\Theta) \mathrm{d}\Theta \tag{6}$$

The optimized bimodal log-normal algorithm was applied universally in YRD (He et al., 2012b; Xia et al., 2007). As described in the Eq. (7), where $\frac{\mathrm{d}V}{\mathrm{d}\ln r}(\mu\mathrm{m}^3\,\mu\mathrm{m}^{-2})$ represents the size distribution, c_i is the column volume concentration r denotes the aerosol radius and r_{mean} is equal to the averages, σ is the standard deviation. The retrieval products provide 22 radius ranges from 0.05 to 15 µm in our study.

$$\frac{\mathrm{d}V}{\mathrm{d}r} = \sum_{i=1}^{2} \frac{c_i}{r\sigma_i\sqrt{2\pi}} \exp\left(-\left(\frac{\ln\left(r/r_{\text{mean},i}\right)}{2\sigma_i^2}\right)^2\right) \tag{7}$$

Usually, some certain single-valued representations of the angular scattering including the asymmetry parameter (g), the up-scatter fraction (b) were used to describe the distribution of scattering (Andrews et al., 2006). In the algorithm, g was computed from scattering angle(Θ) and phase function $p(\Theta)$ in diffuse-sky radiance:

$$g = \langle \cos\Theta \rangle = \frac{1}{2} \int_{-1}^{+1} p(\Theta) \cos\Theta \mathrm{d}(\cos\Theta) \tag{8}$$

As sun-photometer ceased to work in rainy days and the inverted production quality was not guaranteed in too cloudy condition, the available samples in our observation

AMTD
6, 11011–11054, 2013

are described in Table 1. Among them, 10 samples were collected in episodes period. Table 2 lists out the detailed air-pollution episodes dates along with information of AQI and concentration of particulate matter (PM). While daily AQI could serve as a mirror of air pollution level during episodes, hourly averaged PM_{10} and $PM_{2.5}$ were calculated again in the period from 7 a.m. to 6 p.m. in accordance to the observational time of CE318. PM_{10} was assessed as the prominent pollutant in dust days while $PM_{2.5}$ dominated in smoke episodes. What was interesting in Table 2, AQIs in dust days were prevalently lower than those in biomass days. This possibly was a result of the highlighted assessment standard for $PM_{2.5}$ in the updated version of national air quality evaluation system published by Chinese government in 2012.

3 Results and discussions

3.1 Overview of meteorology during dust and biomass burning episodes

Meteorological and environmental conditions are critical indicators of air-pollution episodes and highly-related with aerosol transport and formation mechanisms (Reid et al., 2005). Figure 2 presents the temporal variation of meteorological elements, daily-averaged mass concentrations of particle matter and CO. Backwards air trajectories were also analyzed for dust days using the HYSPLIT-4 (HYbrid Single-Particle Lagrangian Integrated Trajectory) model developed by NOAA/ARL in Fig. 3. Five 72 h back trajectories of each air mass at 500 m arrival height were computed for each day ending at 08:00 UTC in Shanghai (GMT +8). Two types of routes importing dust particles (the major Asian dust source regions of the Gobi desert and Inner Mongolia) are shown in Fig. 3a, among which air masses can even make a detour across Yellow Sea. Meanwhile, the dust particles arriving at the sampling site transported via North China Plain and YRD district, both of which are with dense population and multitudinous industries. This means that it may be mixed with other types aerosols. Although PM data only represents the pollutant concentration in surface level, it still can validate the dust

AMTD
6, 11011–11054, 2013

weather thanks to the mixing effect of boundary layer (Reid et al., 2003). During dust episode, the concentration ratio between PM_{10} and $PM_{2.5}$ surpassed 2 while $PM_{2.5}$ was relatively lower (see in Fig. 2). Take 9 April as a case, abruptly, mass concentrations of $PM_{2.5}$ and PM_{10} climbed up to 52.5 and 149.1 $\mu g\,m^{-3}$ (ratio between PM_{10} and $PM_{2.5}$ was 2.84). The high frequency (more than 60 %) in north-oriented direction is shown in surface wind roses, conformed to the backwards trajectories of air masses at 500 m.

The daily surface firepots derived from MODIS onboard the Terra satellite (Giglio et al., 2003) were plotted in Fig. 3c as an evidence for the occurrence of biomass burning incidents (data from http://earthdata.nasa.gov/data/). Burning smoke aerosols in Shandong and northern Jiangsu Province which began in 18 May occasionally caused an episodic air quality problem in YRD with transport. During the 48 h transportation, the air mass moved slowly from North China Plain and arrived over Shanghai in 20 May. In the condition of crop residue burning pollution episode, daily average mass concentrations of $PM_{2.5}$ and PM_{10} turned out to be 117.5 and 151.2 $\mu g\,m^{-3}$ respectively. The smoke pollution could also be interrelated with the acutely ascending mass concentration of CO (1.21 $mg\,m^{-3}$), which always served as a tracer gas for primary emissions. Other two analogical episodes occurred in June and deteriorated the air quality of Shanghai in 11, 19, 20 June. In these days, the wind turned out to be west-dominant and coincident with the backwards trajectories, blowing the biomass smoke to Shanghai continuously.

3.2 Aerosol Optical Depth and Ångström exponent (α)

AOD is a basic parameter reflecting the air turbidity, the optical extinction capability of aerosol and applied broadly in radiative-climate models and remote sensing research (Chu et al., 2003; Martins et al., 1998; Remer et al., 2005). Defined as the wavelength dependence of the aerosol extinction coefficient, the Ångström exponent (α) is regarded as an optical index reproducing aerosol size distribution (Ångström, 1964). These two parameters are both fundamental to assess the radiative forcing caused by aerosols (Xia et al., 2007). While the enormously spatial variability existed in the

AMTD
6, 11011–11054, 2013

aerosol distribution in YRD, the total extinction of dust, biomass and urban/industrial aerosol was considerable in this region (He et al., 2010). Figure 5 shows the box-chart plot of daily averaged AOD, Ångström exponent (440–870 nm) and water vapor content (WVC) with corresponding standard deviations during the dust and biomass burning days over Shanghai. Samples in days without prominent episodes were collected here to represent the average condition, during which urban/industrial aerosol could be in predominance in the ambient air. We found that the mean of AOD at 440 nm in dust days was 1.06 ± 0.4 in Shanghai and three quarters exceeded 1.0, which increased by a factor of $2 \sim 2.5$ than the yearly $AOD_{440\,nm}$ observed at Dongtan (0.48), Pudong (0.56) (Pan et al., 2010), background site in Linan (0.61) (Xu et al., 2002). But the result was much lower than Beijing (~ 2.7), Zhangye (~ 3.1) and Tengger Desert (2.0 at 550 nm) in China (Huang et al., 2008; Ge et al., 2010; Xin et al., 2005), which may be related to deposition process. During agricultural residue burning episodes, the value of optical thickness at 440 nm yielded 0.72, 15 % higher than the results measured in normal days (~ 0.59). Researchers found that biomass burning smoke contributed a lot in increasing AOD in East China in recent years while presented highly-sensitive characteristics to hygroscopic growth (Li et al., 2007b). The solar extinction ability of smoke particles can be lifted up in the aging process with increasing number density, which was discovered broadly in measurements worldwide (Ogunjobi et al., 2008; Mielonen et al., 2012). However, optical thickness of biomass burning was still much lower than observations during dust outbreaks. Take AOD at 670 nm for example: 75 % in dust days were larger than 0.62 while three quarters of values were less than 0.43 for burning episode. It's worthwhile to note that dust particles imposed extinction effects on the total column atmosphere as it can invade the middle troposhere (Reid et al., 2003).

Universally, the dust aerosols were implied to be mainly in coarse mode with diameter more than 5 µm (Dubovik et al., 2002; Ogunjobi et al., 2004). In our observation, the values of α fluctuated from 0.17 to 0.88 with a mean of 0.74 and standard deviation of 0.16 in dust days. We found that approximately 75 % of α was less than 0.8 and one quarter was even lower than 0.5 (see in Fig. 4), smaller than the seasonally

AMTD
6, 11011–11054, 2013

averaged value (0.87) in April over Shanghai (He et al., 2012b). As deposition progress took place in the long-distance transport, particles with large size were preferentially wiped out, so the α in Shanghai (as far away from dust source regions) were reasonably higher than conclusions got in Dunhuang (0.05) and 0.20 in Yulin (Yu et al., 2006). Differing from dust aerosol, great fraction of fine particles were detected in biomass smoke: the values of α ranged from 0.53 to 1.75 with the average of 1.25, comparable to that obtained in Moldova ($\sim$ 1.14) by Eck et al. (2003). With the ample environmental humidity in summer over Shanghai, water vapor exhibited obviously higher value in burning episode (1.62) in contrast to dusty days (1.08). What should be paid attention to, the condensed water in the ambient air can play a critical role in the hygroscopic growth process of smoke aerosols, enlarging the size of hydrophilic particle (Reid et al., 2005).

Variability of the complex mixture of urban/industrial aerosols turns the distinction of aerosols types (such as inhomogeneous biomass burning smoke and desert dust) to be a harsh challenge (Singh et al., 2004; Xia et al., 2007). However, AOD along with Ångström exponent can be well-used to determine the aerosol types (Dubovik et al., 2002). Figure 5 gives the scatter plot of daily-averaged AOD and α in the observational period (50 samples in total including 5 in dust and 5 in biomass days). Note that high AOD ($>$ 0.85) was almost coupled with low α (approximately less than 0.8) in dust days, coincident with Asian dust property (Kim et al., 2004). Instead, the lower AOD with high α (75 % were larger than 0.9) in non-pollution days demonstrated the predominance of fine particles in Shanghai. The experiment conducted by CSHNET also found the AOD ($\sim$ 0.64 at 500 nm) and α ($\sim$ 1.08) were anticorrelated in Shanghai city (31°12′N, 121°75′E) about 25 km away from FDU. This negative correlation implied that the heavy aerosol loading usually corresponded to large particles, which can be caused by the humidity swelling of sea salt aerosols (Xin et al., 2005). During agricultural crop residue burning incidents, the Ångström exponent presented extremely higher values ($>$ 1.2), associated with moderate AOD values. Eck et al. (2005) figured out that, in the transport of biomass smoke, the reproduced coagulation and contamination along

AMTD
6, 11011–11054, 2013

with aging process could enlarge the particle size and change the relative optical properties. So a comprehensive discussion should be done between the size and optical parameter as shown in Sect. 3.4 in this paper.

The environmental and meteorological elements also impact on the aerosol optical extinction capability by hygroscopic process, photochemical reaction, nucleation (secondary aerosol formation) and so on (Kotchenruther and Hobbs, 1998; Limbeck et al., 2003; Yang et al., 2009). Several observations have validated that the hygroscopic growth process existed in the ambient air with high relative humidity for smoke aerosol (Mochida and Kawamura, 2004; Reid et al., 2005). RH can enhance the particle shift to accumulation mode through condensation, coagulation, resuspension and evolution (He et al., 2012a). When RH shifted from 30 to 80 %, average hygroscopic growth factors for light scattering on the order of 1.3 ∼ 1.5 for biomass smoke (Kotchenruther and Hobbs, 1998). Plotted in Fig. 6, the scatter-plot of Ångström exponent and RH can reveal the biomass smoke aerosol's dependence on condensed water, behaving as a negative correlation. The smoke from agricultural residue burning diluted with industrial/urban aerosol and turned to present bigger sizes after the hygroscopic growth. In contrast, as dust episodes always occur with dry air masses from desserts, so α increased with ascending RH.

3.3 Aerosol size distribution

Similar to AOD and Ångström exponent, aerosol volume spectra is respectably dependent on geographical locations and varies with diverse types (Kim et al., 2004). The column-averaged size distribution of two types aerosols in air-pollution episodes can be described by a bimodal lognormal distribution as depicted in Fig. 7. In normal days, the peak radius of aerosol (fine modes) was around 0.11 µm while the volume concentration reached the second peak at 5.06 µm. The peak radius was larger than results (3.85 µm) derived from AERONET at Taihu site (Xia et al., 2007). He et al. (2012b) discovered that aerosol displayed higher volume concentration in accumulation mode compared to coarse one over Shanghai in all seasons, which was

AMTD
6, 11011–11054, 2013

confirmed in our research by the lower concentration ratio (V_C/V_F ~1.41) between coarse and fine modes. In strong contrast to biomass and urban aerosols, the size distribution during dust periods was significantly dominated by the coarse mode with peak radii at 5 µm and high ratio (~ 3.79) while still far lower than dust source regions such as Bahrain Gulf (~ 10) and Sahara dessert (~ 50) (Dubovik et al., 2002). Smoke particles were considered to be composed of ~ 60 % organic carbon (OC) with ~ 15 % black carbon (BC) and primarily accumulated around 0.2 µm (Reid et al., 2005). For biomass aerosol, the authors found an interesting phenomenon: the radii with magnitude of volume concentration in fine mode (~ 0.15 µm) were larger than those of dust episode and normal days (both at 0.11 µm) and presented higher peak concentration (~ 0.14) than the other two conditions (0.09 and 0.07 for normal and dust). The results were attributed to the dynamic variability of chemical/physical characteristics in observation, during which aged smoke aerosol was discovered to be with larger size than fresh one (Reid et al., 2003). The hygroscopic growth also exerted effect on the amplified particle size in accumulation mode. But at coarse mode, the peak radius (2.13 µm) was severely lagged behind dust and normal conditions (both 5.06 µm) with the lowest concentration. Additionally, the V_C/V_F was nearly to a unit (~ 0.99) in the aerosol size distribution of agricultural residue burning days, which was in good accordance with $PM_{10}/PM_{2.5}$ (see in Fig. 2a). We noted that even in days without prominent episodes, the peak at fine mode was sharper than coarse one. When it comes to early summer in Shanghai, higher temperature with abundant solar radiation accelerate the photochemical reaction process (Ran et al., 2009). Researchers concluded that the gas-formation aerosol mainly consisted with fine particles whose radius was less than 0.02 µm (Huang et al., 2011). These may explain why aerosol was in predominance of fine and accumulation modes over Shanghai in the observational period.

The size distributions varied with different aerosol types and exerted the effect on solar radiation forcing by optical extinction (King et al., 1978). Dust aerosol was always concentrated in coarse mode (shown in Fig. 7) while biomass mainly accumulated in radius less than 2.0 µm (Ge et al., 2010; Kim et al., 2006). To understand the relationship

AMTD
6, 11011–11054, 2013

between number density of these two types aerosols and their optical properties comprehensively, correlativity analysis in three conditions is presented in Fig. 8. Positive relation was found for all types aerosols, which means that the aerosol volume concentration served as a significant contributor to total optical extinction. He et al. (2012b) described the dust aerosol as one type without much account even in highly turbid weather. But according to this study, it should be highlighted that the coarse mode was more correlated with AOD in dust days (correlation coefficient $R \sim 0.77$), signifying the large particles with long-distance transport still impacted a lot on Shanghai aerosol concentration in extreme pollution episodes. In addition to hygroscopic process, Brownian coagulation also took place in the regional transport, accelerating the size growth rate and increasing the concentration (Reid et al., 1998). Dynamic processes often resulted in evolution of the size distribution after the formation of biomass particles, affecting the spectral variation of the optical thickness (Eck et al., 1999). As a result, the volume concentration of smoke was highly-related with aerosol optical extinction in fine mode ($R \sim 0.86$). Generally, fine particles from anthropogenic emissions and secondary aerosol were in majority over Shanghai and presented a more intimate relationship with optical thickness (He et al., 2012b; Limbeck et al., 2003). It can be verified by the fact of higher R (~ 0.82 and ~ 0.88) was calculated out in agricultural residue burning and normal days.

3.4 Aerosol single scattering albedo (ω)

Single scattering albedo is interpreted as an essential parameter indicating the positive or negative radiative forcing. The parameter could be facilitated to determine the aerosol types, widely applied in satellite retrievals (Chu et al., 2003; Levy et al., 2007). Long-distance transport, formation mechanism and meteorological conditions all gave rises to the distribution and magnitude of SSA (Limbeck et al., 2003; Mochida and Kawamura, 2004). The nationwide average of SSA (~ 0.89) in visible band was inversed while the higher value (0.90–0.92) was discovered in eastern China (Li et al., 2007a). Measurements carried out in YRD reported values of SSA at 440 nm fluctuated

AMTD
6, 11011–11054, 2013

from 0.89 to 0.93 in four seasons (Xia et al., 2007). Single scattering albedo from fifty daily samples were made averages at 440, 670, 870 and 1020 nm over Shanghai for dust and biomass burning aerosols in Fig. 9. The ω of dust aerosol showed obvious increasing trend with wavelength, suggesting its stronger scattering capability in visible and IR bands (Dubovik et al., 2002; Ge et al., 2010). As studies pointed out, dust aerosol displayed relatively lower SSA caused by the deposition process during the long-distance transport (Reid et al., 2003). Interestingly, the authors found the average albedo in visible band ($\sim$ 0.92) was higher than Northern China (where was less far from dust source regions) such as Beijing ($\sim$ 0.89) (Yu et al., 2013). A pronounced scattering feature of particles over Shanghai may explain the result to some extend as marine aerosols accounted more here than Northern China cities. Distinctive from dusty days, the magnitude of ω decreased at 670–1020 nm when agricultural residue burning occurred, conformed to similar patterns acquired at other location (Ogunjobi et al., 2004). The added value for biomass burning aerosol at 670 nm compared to that at blue band, which was presumably because of smoldering fires during agriculture work, aging process and hygroscopic growth in the long-range transport (Eck et al., 2003; Reid et al., 2005; Martins et al., 1997). The value of ω at 440 nm ($\sim$ 0.93) was comparable to the result produced in the Shouxian in Anhui province China during agricultural residue burning ($\sim$ 0.92) (Fan et al., 2010), which was also related with the high background scattering index in YRD because of urban/industrial aerosol's impact (Huang et al., 2011). In addition to the polluted aerosols, urban/industrial aerosols, which were from natural and anthropogenic sources in complicated formation and evolution process, behaved different scattering properties in dispersed radiation (Dubovik et al., 2002). In the transport to Shanghai, quite a few of industrial/urban emissions in North China Plain and YRD city clusters enabled the any kinds of aerosols be optically mixed other types (Reid et al., 2005). With the frequent photochemical reactions in summer, secondary aerosol with pronounced scattering ability comes into prominent type, lifting up SSA in Shanghai consequently (Fu et al., 2010). For this, we can see that SSA in days without apparent pollution episodes biased decreasing trend from

AMTD
6, 11011–11054, 2013

visible to NIR band with minute variability, imposing the stable scattering feature in Shanghai. It is worth noting that the SSA at 440 nm was the highest (~ 0.94) in normal condition, which also gave an indication of the greater scattering of solar radiation by fine particles over shorter wavelength (Kim et al., 2004).

Aerosols with distinctive sizes always corresponded to different chemical components, as dust consisted with mineral material, biomass with OC and BC, urban/industrial aerosol with mixed compounds (Kotchenruther and Hobbs, 1998; Limbeck et al., 2003; Yang et al., 2009). As these could generate significant effects on the scattering features, the authors used the size parameter (Ångström exponent) to discuss with scattering ability for different types aerosols. Additionally, considering SSA was the fraction of scattering to total extinction while it determined scattering capability together with AOD, we displayed the scatter plots of SSA · AOD at the wavelength of 440 nm vs. Ångström exponent in all observational days. Unanimous with conclusions got in related research, the magnitude of SSA · AOD decreased with α as an overall result, particles with large size behaved stronger scattering capability in our result (Eck et al., 2005). In general, dust aerosol can be sorted into the type with high scattering capability according to the preceding studies (Ge et al., 2010), which was confirmed in Fig. 10. Although dust particles contributed to cooling effect in level of ground with scattering feature, the top of atmosphere may be warmed up regarding of the increased absorption capability within the atmosphere (Kim et al., 2004). Preceding researches found that smoke aerosol usually was composed of bulks of BC as fine-mode aerosol, which was defined as absorbing type (Holben et al., 1996). However, the results in this plot surprisingly performed high values of α with moderate SSA · AOD for biomass aerosol, showing stronger optical scattering capability than urban/industrial aerosol in normal condition. This was coincident with the fact that AOD in biomass smoke days was more than 10 % higher than averaged one while SSA at 440 nm was nearly same for two conditions. Though fresh biomass aerosol behaved underlying feature of absorption, smoke particles inevitably underwent aging and contamination process in the transport, when chemical and physical properties changed. Reid et al. (2003) found

AMTD
6, 11011–11054, 2013

that less fraction of potassium and BC in aged particles, especially in smoldering combustion. Meanwhile, aged smoke presented more microphysical and chemical properties related to secondary aerosol, such as sulfate with scattering capability increased (Reid et al., 1998). Additionally, the hydrophilic particles in high number density were found to be more featured with light scattering (He et al., 2012a). Furthermore, due to the coastal location of our observation site, water-soluble and sea-salt aerosol frequently transported to Shanghai from the East China Sea and the Yellow Sea. These types aerosols can be mixed with the smoke and resulted in ascending SSA (Koepke et al., 1997; Dubovik et al., 2002; Kim et al., 2001).

3.5 Asymmetry factor (*g*)

Up to now, ground-based retrievals of asymmetry factor were rarely done in Shanghai. The ASY is inversed as the first moment of scattering phase function and biases a fundamental parameter in radiation transfer equation (Dubovik et al., 2002; Andrews et al., 2006). According to the basic definition, ASY is calculated intensity-weighted mean cosine of scattering angle (see in Sect. 2.2). Unity is regarded as a purely forward scattering indicator while zero represents aerosol symmetric scattering (Bergstrom et al., 2003). Various uncertainties existed in this parameter during the inversion as the vague determination of aerosol types (Dubovik and King, 2000). To minimize the uncertainty, the authors depicted averages of ASY at four wavelengths belonging to 50 daily samples (10 in episode condition) in Fig. 11. The *g* showed a decreasing trend at 440–870 nm and then increased weakly in NIR band for dust aerosol. On the other hand, *g* demonstrated a quasi-linear descending relationship at all observed wavelengths for biomass smoke aerosol, denoting its remarkable diversity of forward scattering capability in visible and NIR band. In general, the asymmetry factors in visible band were bout 0.688, 0.693, 0.708 for dust, biomass days and normal days in Shanghai. This phenomenon in our observation highlighted the forward scattering caused by fine particles including biomass smoke and urban aerosol, which may exert warming effects in ground level to some extend. In dusty weather, it revealed the enhancement of the

AMTD
6, 11011–11054, 2013

forward scattering of coarse dust particles in NIR band by the fact of higher values of ASY captured at 1020 nm than biomass smoke (0.652 to 0.625). Based on the fact that AERONET Taihu site was 100 km away from FDU, ASY inverted in averaged condition by us presented lower values. For example, g at 440 nm was 0.719 in the season of Spring (Xia et al., 2007) in the conclusions compared to ours (0.692). Spatial variability existed in YRD district with various types of aerosols in dominance may cause different ASYs in two locations (He et al., 2012a). Taihu area facilitates as China's major manufacturing base with numerous small privately owned factories emitting huge amounts of pollutants while Shanghai is affected by complicated urban/industrial aerosol considerably (Xin et al., 2005). The insoluble species in urban/industrial aerosol are mostly soil particles with certain amount of organic material. Besides, the water soluble component that originated from gas to particle conversion contains various kinds of sulfate, nitrate, and other organics (Hess et al., 1998). More in situ experiments should be operated to capture the regional variations of asymmetry factors belonging to aerosols of respective type.

3.6 Validation with AOD from MODIS

High surface reflectance and variable aerosol types with distinctive optical properties can determine the retrieval accuracy in satellite remote sensing (Chu et al., 2003). For a long time, coexistence of dust, smoke and urban/industrial aerosols over China confused satellite retrievals (Li et al., 2007b). During the inversion of MODIS Collection 051 products, the algorithm set aerosol as three types according to SSA: nonabsorbing (~ 0.95), moderately absorbing (~ 0.90) and absorbing (~ 0.85) (Levy et al., 2007). Dust can be classified as weakly absorbing type while biomass as absorbing one in southeast Asia area (Che et al., 2009). Fine mode fraction aerosol accounted 40 % to 60 % in East China, which were mainly emitted from natural and anthropogenic sources and possibly consisted of soil dust, biomass smoke and urban/industrial type (He et al., 2012a). We made spatial averages (40 km × 40 km) of MODIS AOD at 550 nm while temporally-mean (±30 min when satellite passed) AOD interpolated from 440

AMTD
6, 11011–11054, 2013

and 670 nm observed by CE318. The validation results turned to be a barely satisfactory for no episode condition, in which 75 % samples were in the above error range ($\Delta\tau = 0.2\tau + 0.05$). As shown in Fig. 12, among all validations (36 samples), the authors found that the overestimation of AOD in clear condition in contrast to underestimation for polluted aerosol still existed obviously as a common phenomenon (Remer et al., 2005). The deviation of the MODIS AOD from ground-based results were mainly due to aerosol model assumptions, where SSA varied with dust, smoke, urban/industrial and marine aerosols (Dubovik et al., 2002). This parameter was fixed from 0.95 to 0.85 in MODIS inversion since Collection 005 algorithm in East China region (Mi et al., 2007). However, coastal location gave rises to water-soluble and sea-salt in ambient air, enhancing the scattering property of regional aerosol in Shanghai (He et al., 2012b). Meanwhile, the performance of the MODIS C051 product changed with surface reflectance. Bright surfaces such as urban areas and desserts always brought about overestimations as more absorption was considered in the retrievals. So the results in clear days (6 samples) were outside the accepted error range. The East Asian Tropospheric Aerosol experiment outlined the SSA in YRD (~ 0.93) exceeding the results in Beijing (~ 0.81) and Guangzhou (~ 0.85) (Li et al., 2007a), but the concrete values were still blank for biomass and dust over Shanghai. The absence of accurate SSA may result in the underestimation of AOD in episode days (He et al., 2010). With our effort (results presented in Sects. 3.2–3.4), the revisions could be conducted using the refreshed parameters to improve the accuracy of regional MODIS retrievals.

4 Conclusions and discussions

Based on the three-month observation over Shanghai from 28 March to 25 June in 2013, this paper retrieved aerosol optical parameters utilizing ground-based sunphotometer. Thus far, according to what we were informed, no comparative investigations about different aerosol types in YRD were operated. While aerosol optical properties varied with temporal and spatial distribution (He et al., 2010), both common and

AMTD
6, 11011–11054, 2013

diverse characteristics of aerosols were presented in this study compared to former researches. Ascending aerosol loadings were found in dusty (~ 1.06 at 440 nm) and burning (~ 0.72 at 440 nm) days in contrast to normal days (~ 0.59 at 440 nm). AOD along with Ångström exponent were used to distinguish the aerosol types, further characterizing the optical properties belonging to various types. Small value of α for dust aerosol (three quarters $\leq$ 0.8) with extremely low value (< 0.5) occurred in dust periods, imposing the strong extinction capability of coarse dust particles. Biomass smoke was discovered to display moderate AOD coupled with high α (1.06 as average). As high humidity in Shanghai gave rise to hydrophilic aerosols, the authors also analyzed and found a negative relationship between RH and Ångström exponent in biomass days.

The aerosol volume size distribution exhibited the bimodal logarithm normal structure in all conditions in our study over Shanghai. Dust particles were concentrated in coarse mode (~ 5 µm) while biomass aerosol primarily accumulated in fine mode (~ 0.17 µm). Positive correlation coefficient (R) was demonstrated between AOD with volume concentration for all types aerosols, implying the particle concentration could serve as a vital contributor to total optical extinction. Higher R (~ 0.82 and ~ 0.88) was calculated out in agricultural residue burning and normal days, which imposed that fine particles from anthropogenic emissions and secondary aerosols may play the key role in optical extinction process. What should be highlighted, dust particles through long-distance transport still impacted considerably in extreme pollution episodes as the R (~ 0.77) in coarse mode was higher than those of smoke (~ 0.71) and average condition (~ 0.76).

The value of single scattering albedo during biomass burning displayed a variation from 0.902 to 0.922 with a descending trend at 670–1020 nm, while SSA increased with wavelength for dust aerosol. The negative correlation between SSA · AOD and Ångström exponent was analyzed to show the order of scattering capability: urban/industrial < biomass < dust aerosols. Higher value of asymmetry factor in longer wavelength of dust aerosol (~ 0.652 at 1020 nm) was found compared to average condition and biomass smoke (both equaled to 0.625), suggesting the enhancing forward

AMTD
6, 11011–11054, 2013

scattering by dust in NIR band. This refreshed parameter could be fixed in optimizing aerosol models serving for radiation transfer equation (Andrews et al., 2006). As SSA was a key parameter determining the aerosol types in retrieval algorithm (Collection 051), the validation of AOD vs. MODIS reflected the errors for dust and biomass types aerosols, which may be attributed to the variable SSA in YRD (He et al., 2010). The ascending deviation also existed in clear condition caused by overestimation of ground reflectance (Chu et al., 2003; Levy et al., 2007).

During our measurement, some points are worth noting: as the site is located in the city center and the observation was conducted in ambient air, mixture with various types of aerosols inevitably affected the result in this paper. For example, vehicle emission in Shanghai has become a major source of urban air pollution with over 10 % increasing rate of vehicle population annually since 2001 (Wang et al., 2012). Although we collected samples in no-episode days as background condition, which may represent the urban/industrial aerosol, it still calls for extensive laboratory and in situ experiments for single type aerosol's property.

Acknowledgements. This work was partially supported by the National Natural Science Foundation of China under grant No. 21277029, 40975076, Science and Technology Commission of Shanghai Municipality (Grant: 12DJ1400102), and China Meteorological Administration (Grant: GYHY201106045-8). We also thank the support of National Hightech R&D Program ("863" Program, No. 2006AA06Z417). We gratefully acknowledge the NOAA Air Resources Laboratory (ARL) for provision of the HYSPLIT trajectory model for public use. Great thanks owe to MODIS technical team who granted us with firemap and AOD in real time. We also would like to extend our sincere thanks to Shanghai Environmental Monitoring Center for the fresh publication of AQI data.

References

Andrews, E., Sheridan, P., Fiebig, M., McComiskey, A., Ogren, J., Arnott, P., Covert, D., Elleman, R., Gasparini, R., and Collins, D.: Comparison of methods for deriving aerosol asymmetry parameter, J. Geophys. Res., 111, D05S04, doi:10.1029/2004JD005734, 2006.

Ångström, A.: The parameters of atmospheric turbidity, Tellus, 16, 64–75, 1964.
Badarinath, K., Kharol, S. K., Kaskaoutis, D., and Kambezidis, H.: Influence of atmospheric aerosols on solar spectral irradiance in an urban area, J. Atmos. Sol.-Terr. Phy., 69, 589–599, 2007.
Bergstrom, R. W., Pilewskie, P., Schmid, B., and Russell, P. B.: Estimates of the spectral aerosol single scattering albedo and aerosol radiative effects during SAFARI 2000, J. Geophys. Res., 108, 8474, doi:10.1029/2002JD002435, 2003.
Che, H., Zhang, X., Chen, H., Damiri, B., Goloub, P., Li, Z., Zhang, X., Wei, Y., Zhou, H., and Dong, F.: Instrument calibration and aerosol optical depth validation of the China Aerosol Remote Sensing Network, J. Geophys. Res., 114, DS03206, doi:10.1029/2008JD011030, 2009.
Chu, D. A., Kaufman, Y., Zibordi, G., Chern, J., Mao, J., Li, C., and Holben, B.: Global monitoring of air pollution over land from the Earth Observing System Terra Moderate Resolution Imaging Spectroradiometer (MODIS), J. Geophys. Res., 108, 4661, doi:10.1029/2002JD003179, 2003.
Dubovik, O. and King, M. D.: A flexible inversion algorithm for retrieval of aerosol optical properties from Sun and sky radiance measurements, J. Geophys. Res., 105, 20673–20696, 2000.
Dubovik, O., Holben, B., Eck, T. F., Smirnov, A., Kaufman, Y. J., King, M. D., Tanré, D., and Slutsker, I.: Variability of absorption and optical properties of key aerosol types observed in worldwide locations, J. Atmos. Sci., 59, 590–608, 2002a.
Dubovik, O., Holben, B., Lapyonok, T., Sinyuk, A., Mishchenko, M., Yang, P., and Slutsker, I. Nonspherical aerosol retrieval method employing light scattering by spheroids, Geophys. Res. Lett., 29, 51–54, 2002b.
Dubovik, O., Sinyuk, A., Lapyonok, T., Holben, B. N., Mishchenko, M., Yang, P., Eck, T. F., Volten, H., Muñoz, O., and Veihelmann, B.: Application of spheroid models to account for aerosol particle nonsphericity in remote sensing of desert dust, J. Geophys. Res., 111, D11208, doi:10.1029/2005JD006619, 2006.
Eck, T., Holben, B., Reid, J., Dubovik, O., Smirnov, A., O'Neill, N., Slutsker, I., and Kinne, S.: Wavelength dependence of the optical depth of biomass burning, urban, and desert dust aerosols, J. Geophys. Res.-Atmos., 104, 31333–31349, 1999.
Eck, T., Holben, B., Reid, J., O'Neill, N., Schafer, J., Dubovik, O., Smirnov, A., Yamasoe, M., and Artaxo, P.: High aerosol optical depth biomass burning events: a compar-

AMTD
6, 11011–11054, 2013

ison of optical properties for different source regions, Geophys. Res. Lett., 30, 2035, doi:10.1029/2003GL017861, 2003.
Eck, T., Holben, B., Dubovik, O., Smirnov, A., Goloub, P., Chen, H., Chatenet, B., Gomes, L., Zhang, X. Y., and Tsay, S. C.: Columnar aerosol optical properties at AERONET sites in central eastern Asia and aerosol transport to the tropical mid-Pacific. J. Geophys. Res., 110, D06202, doi:10.1029/2004JD005274, 2005.
Fan, X., Chen, H., Xia, X., Li, Z., and Cribb, M.: Aerosol optical properties from the Atmospheric Radiation Measurement Mobile Facility at Shouxian, China. J. Geophys. Res., 115, D00K33, doi:10.1029/2010JD014650, 2010.
Fu, Q., Zhuang, G., Wang, J., Xu, C., Huang, K., Li, J., Hou, B., Lu, T., and Streets, D. G.: Mechanism of formation of the heaviest pollution episode ever recorded in the Yangtze River Delta, China, Atmos. Environ., 42, 2023–2036, 2008.
Fu, Q., Zhuang, G., Li, J., Huang, K., Wang, Q., Zhang, R., Fu, J., Lu, T., Chen, M., and Wang, Q.: Source, long-range transport, and characteristics of a heavy dust pollution event in Shanghai, J. Geophys. Res., 115, D00K29, doi:10.1029/2009JD013208, 2010.
Gao, J., Wang, T., Zhou, X., Wu, W., and Wang, W.: Measurement of aerosol number size distributions in the Yangtze River delta in China: formation and growth of particles under polluted conditions, Atmos. Environ., 43, 829–836, 2009.
Ge, J., Su, J., Ackerman, T., Fu, Q., Huang, J., and Shi, J.: Dust aerosol optical properties retrieval and radiative forcing over northwestern China during the 2008 China-US joint field experiment, J. Geophys. Res., 115, D00K12, doi:10.1029/2009JD013263, 2010.
Giglio, L., Descloitres, J., Justice, C. O., and Kaufman, Y. J.: An enhanced contextual fire detection algorithm for MODI S. Remote Sens. Environ., 87, 273–282, 2003.
Haywood, J. and Boucher, O.: Estimates of the direct and indirect radiative forcing due to tropospheric aerosols: a review, Rev. Geophys., 38, 513–543, 2000.
He, Q., Li, C., Tang, X., Li, H., Geng, F., and Wu, Y.: Validation of MODIS derived aerosol optical depth over the Yangtze River Delta in China, Remote Sens. Environ., 114, 1649–1661, 2010.
He, Q., Li, C., Geng, F., Lei, Y., and Li, Y.: Study on Long-term Aerosol Distribution over the Land of East China Using MODIS Data, Aerosol and Air Quality Research, 12, 304–319, 2012a.
He, Q., Li, C., Geng, F., Yang, H., Li, P., Li, T., Liu, D., and Pei, Z.: Aerosol optical properties retrieved from Sun photometer measurements over Shanghai, China, J. Geophys. Res., 117, D16204, doi:10.1029/2011JD017220, 2012b.

AMTD
6, 11011–11054, 2013

Hess, M., Koepke, P., and Schult, I.: Optical properties of aerosols and clouds: the software package OPAC, B. Am. Meteorol. Soc., 79, 831–844, 1998.
Holben, B., Setzer, A., Eck, T., Pereira, A., and Slutsker, I.: Effect of dry-season biomass burning on Amazon basin aerosol concentrations and optical properties, 1992–1994, J. Geophys. Res., 101, 19465–19481, 1996.
Huang, C., Chen, C. H., Li, L., Cheng, Z., Wang, H. L., Huang, H. Y., Streets, D. G., Wang, Y. J., Zhang, G. F., and Chen, Y. R.: Emission inventory of anthropogenic air pollutants and VOC species in the Yangtze River Delta region, China, Atmos. Chem. Phys., 11, 4105–4120, doi:10.5194/acp-11-4105-2011, 2011.
Huang, K., Zhuang, G., Lin, Y., Li, J., Sun, Y., Zhang, W., and Fu, J. S.: Relation between optical and chemical properties of dust aerosol over Beijing, China, J. Geophys. Res., 115, D00K16, doi:10.1029/2003JD003550, 2010.
Huang, Y., Li, L., Li, J., Wang, X., Chen, H., Chen, J., Yang, X., Gross, D. S., Wang, H., Qiao, L., and Chen, C.: A case study of the highly time-resolved evolution of aerosol chemical and optical properties in urban Shanghai, China, Atmos. Chem. Phys., 13, 3931–3944, doi:10.5194/acp-13-3931-2013, 2013.
Jacobson, M. Z.: Strong radiative heating due to the mixing state of black carbon in atmospheric aerosols, Nature, 409, 695–697, 2001.
Jinhuan, Q. and Liquan, Y.: Variation characteristics of atmospheric aerosol optical depths and visibility in North China during 1980–1994, Atmos. Environ., 34, 603–609, 2000.
Kaufman, Y., Tanré, D., Dubovik, O., Karnieli, A., and Remer, L.: Absorption of sunlight by dust as inferred from satellite and ground-based remote sensing, Geophys. Res. Lett., 28, 1479–1482, 2001.
Kim, D. H., Sohn, B. J., Nakajima, T., Takamura, T., Takemura, T., Choi, B. C., and Yoon, S. C.: Aerosol optical properties over East Asia determined from ground-based sky radiation measurements, J. Geophys. Res., 109, D02209, doi:10.1029/2003JD003387, 2004.
Kim, J., Yoon, S.-C., Jefferson, A., and Kim, S.-W.: Aerosol hygroscopic properties during Asian dust, pollution, and biomass burning episodes at Gosan, Korea in April 2001, Atmos. Environ., 40, 1550–1560, 2006.
King, M. D., Byrne, D. M., Herman, B. M., and Reagan, J. A.: Aerosol size distributions obtained by inversions of spectral optical depth measurements, J. Atmos. Sci., 35, 2153–2167, 1978.
Köpke, P., Hess, M., Schult, I., and Shettle, E.: Global Aerosol Data Set, Max-Planck-Institut für Meteorologie, Hamburg, Germany, 1997.

AMTD
6, 11011–11054, 2013

Kotchenruther, R. A. and Hobbs, P. V.: Humidification factors of aerosols from biomass burning in Brazil, J. Geophys. Res.-Atmos., 103, 32081–32089, 1998.
Lei, Y., Zhang, Q., He, K. B., and Streets, D. G.: Primary anthropogenic aerosol emission trends for China, 1990–2005, Atmos. Chem. Phys., 11, 931–954, doi:10.5194/acp-11-931-2011, 2011.
Levy, R. C., Remer, L. A., and Dubovik, O.: Global aerosol optical properties and application to Moderate Resolution Imaging Spectroradiometer aerosol retrieval over land, J. Geophys. Res., 112, D13210, doi:10.1029/2006JD007815, 2007.
Li, H., Han, Z., Cheng, T., Du, H., Kong, L., Chen, J., Zhang, R., and Wang, W.: Agricultural fire impacts on the air quality of Shanghai during summer harvesttime, Aerosol and Air Quality Resarch, 10, 95–101, 2010.
Li, Z., Goloub, P., Devaux, C., Gu, X., Qiao, Y., Zhao, F., and Chen, H.: Aerosol polarized phase function and single-scattering albedo retrieved from ground-based measurements, Atmos. Res., 71, 233–241, 2004.
Li, Z., Chen, H., Cribb, M., Dickerson, R., Holben, B., Li, C., Lu, D., Luo, Y., Maring, H., and Shi, G.: Preface to special section on East Asian Studies of Tropospheric Aerosols: An International Regional Experiment (EAST-AIRE). J. Geophys. Res., 112, D22S00, doi:10.1029/2007JD008479, 2007a.
Limbeck, A., Kulmala, M., and Puxbaum, H.: Secondary organic aerosol formation in the atmosphere via heterogeneous reaction of gaseous isoprene on acidic particles, Geophys. Res. Lett., 30, 1996, doi:10.1029/2003GL017738, 2003.
Lu, Z., Zhang, Q., and Streets, D. G.: Sulfur dioxide and primary carbonaceous aerosol emissions in China and India, 1996–2010, Atmos. Chem. Phys., 11, 9839–9864, doi:10.5194/acp-11-9839-2011, 2011.
Martins, J. V., Artaxo, P., Liousse, C., Reid, J. S., Hobbs, P. V., and Kaufman, Y. J.: Effects of black carbon content, particle size, and mixing on light absorption by aerosols from biomass burning in Brazil, J. Geophys. Res., 103, 32041–32050, 1998.
Metz, B., Davidson, O., Bosch, P., Dave, R., and Meyer, L.: IPCC: Climate Change 2007: Mitigation, Contribution of Working Group III to the Fourth Assessment Report of the Intergovernmental Panel on Climate Change, Cambridge University Press, Cambridge, UK and New York, NY, USA, 2007.

AMTD
6, 11011–11054, 2013

Mi, W., Li, Z., Xia, X., Holben, B., Levy, R., Zhao, F., Chen, H., and Cribb, M.: Evaluation of the moderate resolution imaging spectroradiometer aerosol products at two aerosol robotic network stations in China, J. Geophys. Res., 112, D22S08, doi:10.1029/2007JD008474, 2007.
Mielonen, T., Portin, H., Komppula, M., Leskinen, A., Tamminen, J., Ialongo, I., Hakkarainen, J., Lehtinen, K., and Arola, A.: Biomass burning aerosols observed in Eastern Finland during the Russian wildfires in summer 2010 – Part 2: Remote sensing, Atmos. Environ., 47, 279–287, 2012.
Mochida, M. and Kawamura, K.: Hygroscopic properties of levoglucosan and related organic compounds characteristic to biomass burning aerosol particles, J. Geophys. Res., 109, D21202, doi:10.1029/2004JD004962, 2004.
Mugnai, A. and Wiscombe, W. J.: Scattering from nonspherical Chebyshev particles, I: cross sections, single-scattering albedo, asymmetry factor, and backscattered fraction, Appl. Optics, 25, 1235–1244, 1986.
Ogunjobi, K., He, Z., Kim, K., and Kim, Y.: Aerosol optical depth during episodes of Asian dust storms and biomass burning at Kwangju, South Korea, Atmos. Environ., 38, 1313–1323, 2004.
Pan, L., Che, H., Geng, F., Xia, X., Wang, Y., Zhu, C., Chen, M., Gao, W., and Guo, J.: Aerosol optical properties based on ground measurements over the Chinese Yangtze Delta Region, Atmos. Environ., 44, 2587–2596, 2010.
Ramanathan, V., Crutzen, P. J., Lelieveld, J., Mitra, A., Althausen, D., Anderson, J., Andreae, M., Cantrell, W., Cass, G., and Chung, C.: Indian Ocean Experiment: an integrated analysis of the climate forcing and effects of the great Indo-Asian haze, J. Geophys. Res.-Atmos., 106, 28371–28398, 2001.
Ran, L., Zhao, C., Geng, F., Tie, X., Tang, X., Peng, L., Zhou, G., Yu, Q., Xu, J., and Guenther, A.: Ozone photochemical production in urban Shanghai, China: Analysis based on ground level observations, J. Geophys. Res.-Atmos., 114, D15301, doi:10.1029/2008JD010752, 2009.
Reid, J. S., Hobbs, P. V., Liousse, C., Martins, J. V., Weiss, R. E., and Eck, T. F.: Comparisons of techniques for measuring shortwave absorption and black carbon content of aerosols from biomass burning in Brazil, J. Geophys. Res.-Atmos., 103, 32031–32040, 1998.
Reid, J. S., Kinney, J. E., Westphal, D. L., Holben, B. N., Welton, E. J., Tsay, S. C., Eleuterio, D. P., Campbell, J. R., Christopher, S. A., and Colarco, P.: Analysis of measurements of Saharan dust by airborne and ground-based remote sensing methods dur-

AMTD
6, 11011–11054, 2013

ing the Puerto Rico Dust Experiment (PRIDE), J. Geophys. Res.-Atmos., 108, 8586, doi:10.1029/2002JD002493, 2003.
Reid, J. S., Koppmann, R., Eck, T. F., and Eleuterio, D. P.: A review of biomass burning emissions part II: intensive physical properties of biomass burning particles, Atmos. Chem. Phys., 5, 799–825, doi:10.5194/acp-5-799-2005, 2005.
Remer, L. A., Kaufman, Y., Tanré, D., Mattoo, S., Chu, D., Martins, J., Li, R.-R., Ichoku, C., Levy, R., and Kleidman, R.: The MODIS aerosol algorithm, products, and validation, J. Atmos. Sci., 62, 947–973, 2005.
Russell, P. B., Hobbs, P. V., and Stowe, L. L.: Aerosol properties and radiative effects in the United States east coast haze plume: An overview of the Tropospheric Aerosol Radiative Forcing Observational Experiment (TARFOX), J. Geophys. Res., 104, 2213–2222, 1999.
Shindell, D. and Faluvegi, G.: Climate response to regional radiative forcing during the twentieth century, Nat. Geosci., 2, 294–300, 2009.
Singh, R., Dey, S., Tripathi, S., Tare, V., and Holben, B.: Variability of aerosol parameters over Kanpur, northern India. J. Geophys. Res.-Atmos., 109, D23206, doi:10.1029/2004JD004966, 2004.
Takemura, T., Nakajima, T., Dubovik, O., Holben, B. N., and Kinne, S.: Single-scattering albedo and radiative forcing of various aerosol species with a global three-dimensional model, J. Climate, 15, 333–352, 2002.
Takemura, T., Nozawa, T., Emori, S., Nakajima, T. Y., and Nakajima, T.: Simulation of climate response to aerosol direct and indirect effects with aerosol transport-radiation model, J. Geophys. Res.-Atmos., 110, D02202, doi:10.1029/2004JD005029, 2005.
Wang, J., Guo, P., Li, X., Zhu, J., Reinert, T., Heitmann, J., Spemann, D., Vogt, J., Flagmeyer, R.-H., and Butz, T.: Source identification of lead pollution in the atmosphere of Shanghai City by analyzing single aerosol particles (SAP), Environ. Sci. Technol., 34, 1900–1905, 2000.
Wang, S., Zhou, B., Wang, Z., Yang, S., Hao, N., Valks, P., Trautmann, T., and Chen, L.: Remote sensing of NO2 emission from the central urban area of Shanghai (China) using the mobile DOAS technique, J. Geophys. Res.-Atmos., 117, D13305, doi:10.1029/2011JD016983, 2012.
Wang, X., Zhang, Y., Chen, H., Yang, X., Chen, J., and Geng, F.: Particulate nitrate formation in a highly polluted urban area: A case study by single-particle mass spectrometry in Shanghai, Environ. Sci. Technol., 43, 3061–3066, 2009.

AMTD
6, 11011–11054, 2013

Wang, Y., Zhuang, G., Zhang, X., Huang, K., Xu, C., Tang, A., Chen, J., and An, Z.: The ion chemistry, seasonal cycle, and sources of $PM_{2.5}$ and TSP aerosol in Shanghai, Atmos. Environ., 40, 2935–2952, 2006.

Westerdahl, D., Wang, X., Pan, X., and Zhang, K. M.: Characterization of on-road vehicle emission factors and microenvironmental air quality in Beijing, China, Atmos. Environ., 43, 697–705, 2009.

Xia, X., Li, Z., Holben, B., Wang, P., Eck, T., Chen, H., Cribb, M., and Zhao, Y.: Aerosol optical properties and radiative effects in the Yangtze Delta region of China, J. Geophys. Res., 112, D22S12, doi:10.1029/2007JD008859, 2007.

Xin, J., Wang, S., Wang, Y., Yuan, J., Zhang, W., and Sun, Y.: Optical properties and size distribution of dust aerosols over the Tengger Desert in Northern China, Atmos. Environ., 39, 5971–5978, 2005.

Xu, J., Bergin, M., Yu, X., Liu, G., Zhao, J., Carrico, C., and Baumann, K.: Measurement of aerosol chemical, physical and radiative properties in the Yangtze delta region of China, Atmos. Environ., 36, 161–173, 2002.

Xue, Y., Xu, H., Li, Y., Yang, L., Mei, L., Guang, J., Hou, T., He, X., Dong, J., Chen, Z., and Qi, Y.: Long-term aerosol optical depth datasets over China retrieved from satellite data, Atmos. Meas. Tech. Discuss., 4, 6643–6678, doi:10.5194/amtd-4-6643-2011, 2011.

Ye, B., Ji, X., Yang, H., Yao, X., Chan, C. K., Cadle, S. H., Chan, T., and Mulawa, P. A.: Concentration and chemical composition of $PM_{2.5}$ in Shanghai for a 1-year period, Atmos. Environ., 37, 499–510, 2003.

Yu, X., Cheng, T., Chen, J., and Liu, Y.: A comparison of dust properties between China continent and Korea, Japan in East Asia, Atmos. Environ., 40, 5787–5797, 2006.

Yu, X., Shi, C., Ma, J., Zhu, B., Li, M., Wang, J., Yang, S., and Kang, N.: Aerosol optical properties during firework, biomass burning and dust episodes in Beijing, Atmos. Environ., 81, 475–484, doi:10.1016/j.atmosenv.2013.08.067, 2013.

Zhang, T., Cao, J., Tie, X., Shen, Z., Liu, S., Ding, H., Han, Y., Wang, G., Ho, K., and Qiang, J.: Water-soluble ions in atmospheric aerosols measured in Xi'an, China: Seasonal variations and sources, Atmos. Res., 102, 110–119, 2011.

AMTD
6, 11011–11054, 2013

Table 1. Number of validated sample[a] *s* in the observation period since 28 March to 25 June.

Month	Mar	Apr	May	Jun	Total
Samples	4	22	15	9	50

[a] CE318 ceased to observe in rainy days.

AMTD
6, 11011–11054, 2013

Table 2. The Air Quality Index and mass concentration of particulate matter of selected episode days in this study.

Episode	Date	AQI (24 h)[a]	Prominent pollutant	$PM_{2.5}$[b]/μg m^3	PM_{10}/μg m^3
Dust	30 Mar 2013	53	PM_{10}	31.69	79.82
	8 Apr 2013	97	PM_{10}	57.06	141.51
	9 Apr 2013	94	PM_{10}	69.25	140.92
	10 Apr 2013	107	PM_{10}	57.58	143.39
	17 Apr 2013	128	PM_{10}	70.66	164.88
Biomass Burning	20 May 2013	152	$PM_{2.5}$	106.51	120.39
	21 May 2013	122	$PM_{2.5}$	117.47	151.20
	11 Jun 2013	163	$PM_{2.5}$	114.38	133.35
	12 Jun 2013	158	$PM_{2.5}$	12219	140.38
	19 Jun 2013	129	$PM_{2.5}$	112.32	150.37

[a] Daily AQI was calculated according to national standard 2012 put forward by Chinese government.
[b] Average concentrations of $PM_{2.5}$ and PM_{10} were calculated using hourly-averaged data from 7 a.m. to 6 p.m. in each observation day as CE318 mainly worked in this period.

AMTD
6, 11011–11054, 2013

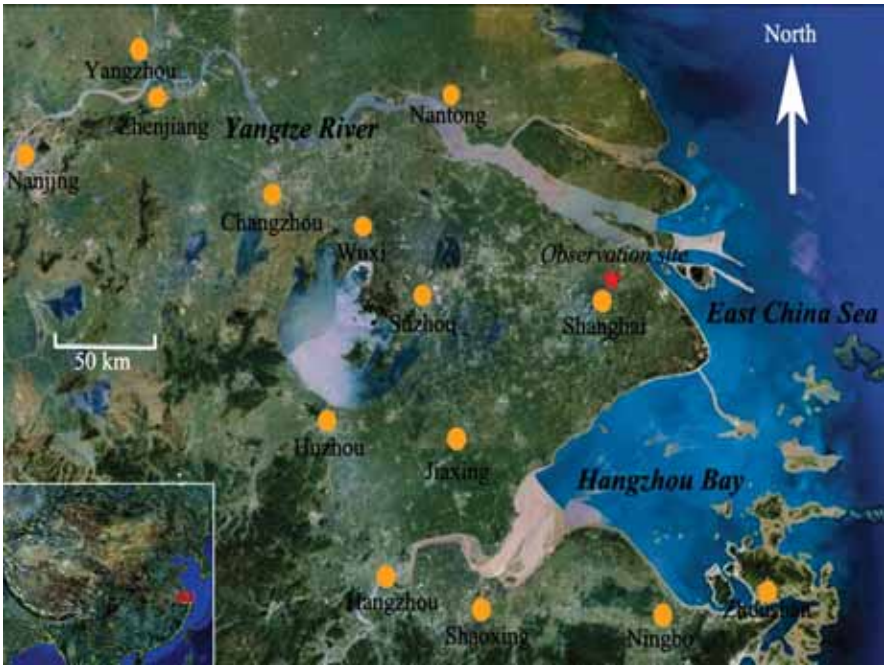

Fig. 1. Geographical location of observation site at Fudan University located in Shanghai from Google Earth.

AMTD
6, 11011–11054, 2013

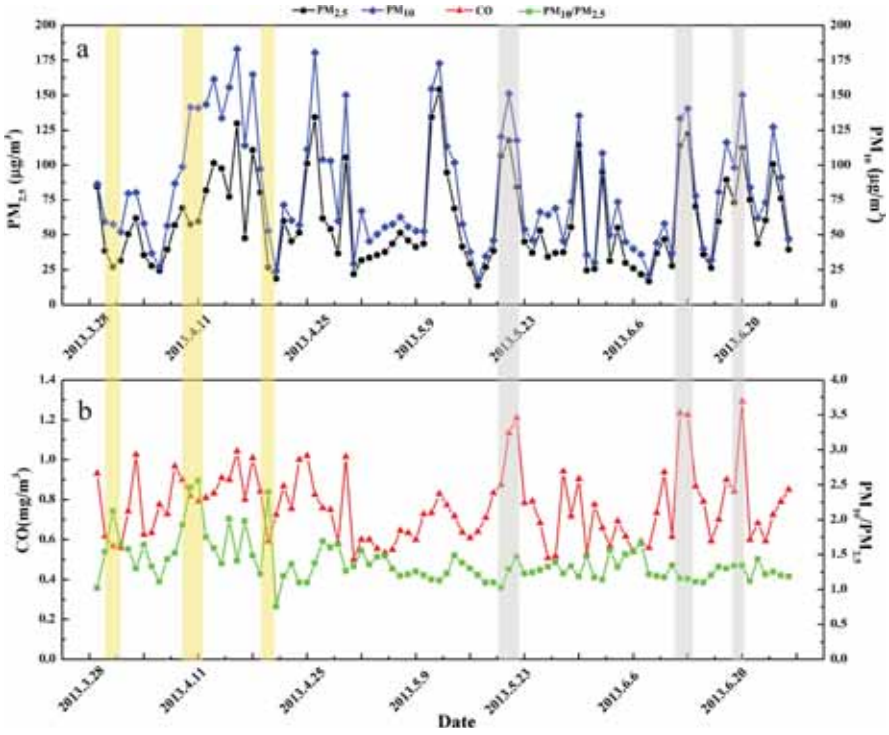

Fig. 2. Temporal variations of **(a)**.daily-averaged mass concentrations of PM_{10}, $PM_{2.5}$ and **(b)**. daily-averaged mass concentrations of CO, ratios between PM_{10},$PM_{2.5}$ in observation period from 28 March to 25 June. Five dust days were in brown shadow while five biomass burning days were grey-shadowed.

AMTD
6, 11011–11054, 2013

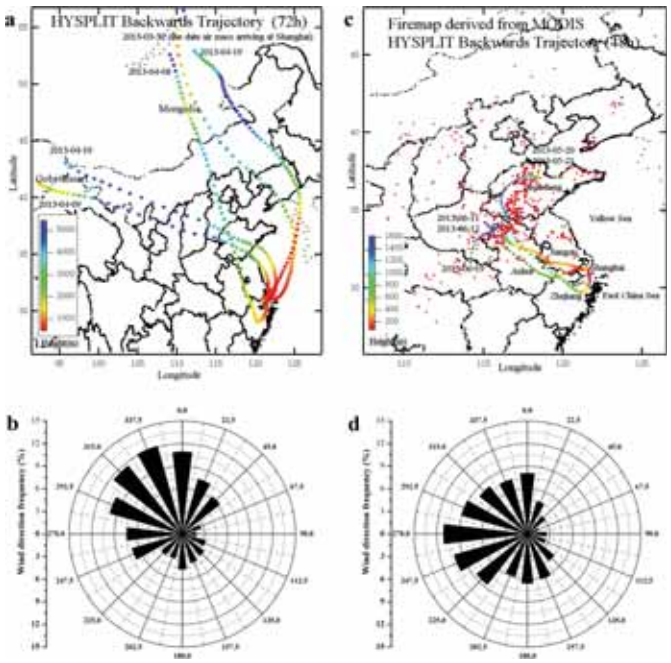

Fig. 3. Backward trajectories based on HYSPLIT model and firemaps derived from MODIS with wind roses during observation period. **(a)** Hourly resolved 72 h air mass back trajectories during dust episodes (five days); **(b)** wind roses during five dust days using hourly-averaged data for analysis; **(c)** hourly resolved 48 h air mass trajectory with daily firepots derived from MODIS during biomass burning episode (five days); **(d)**. Wind roses during five biomass burning days using hourly-averaged data for analysis.

AMTD
6, 11011–11054, 2013

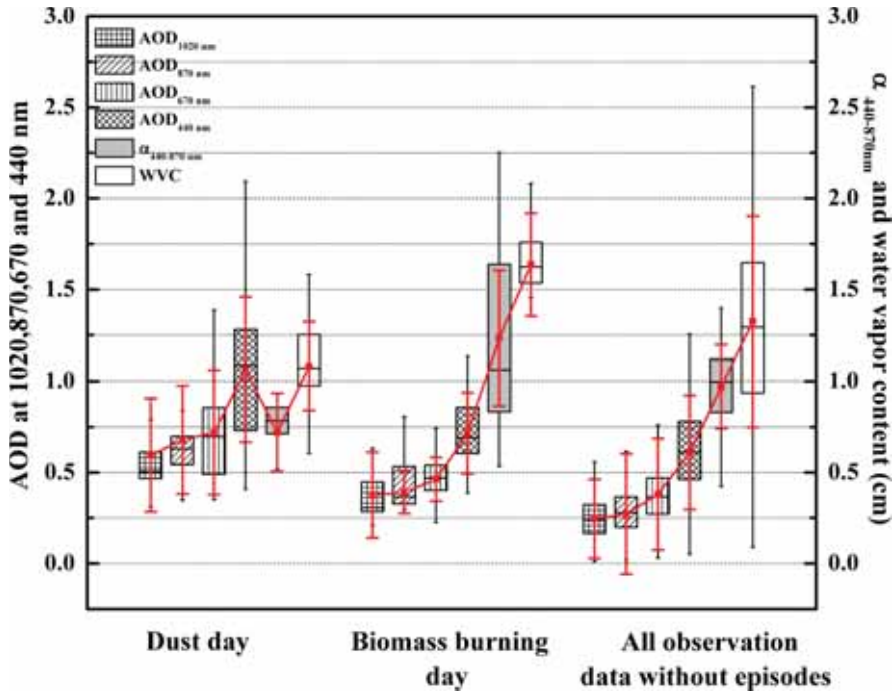

Fig. 4. Box-chart plot of AOD at four wavelengths and Ångström exponent, water vapor content in the observation period over Shanghai. The top and bottom of the box refer to 75 %, 25 % dividing line while the middle line refers to median value in our observation. The red points with corresponding lines refer to the all-averaged AOD with standard deviations calculated from all hourly-averaged AODs in dust (five days), biomass burning (five days) episodes and 40 normal days.

AMTD
6, 11011–11054, 2013

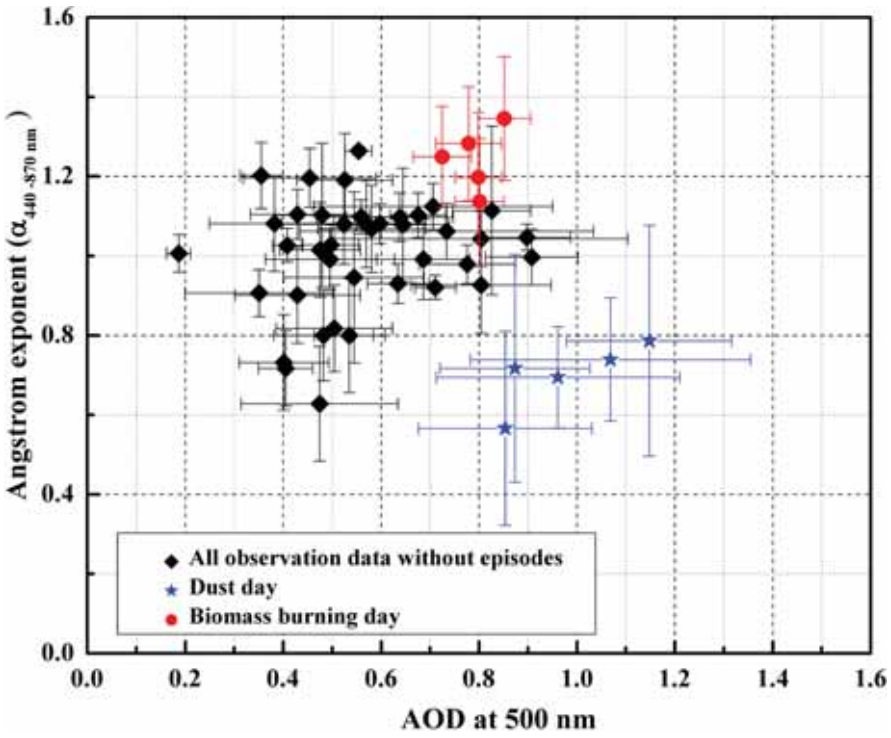

Fig. 5. Scatterplot of daily-averaged AOD at 500 nm and Ångström exponent in the observation period over Shanghai. The averages with standard deviation were calculated from all inversed AOD and Ångström exponent in each observation day. Five samples were for dust (in blue) and five samples were for biomass (in red) while forty samples represented normal condition (in black).

AMTD
6, 11011–11054, 2013

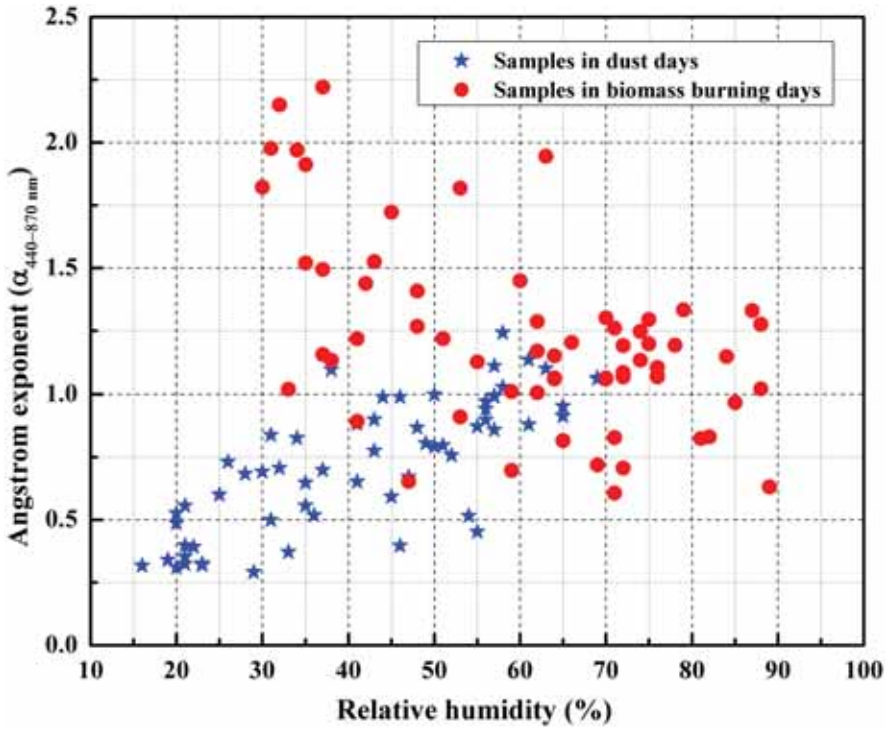

Fig. 6. Scatterplot of hourly-averaged relative humidity and Ångström exponent in dust (in blue) and biomass burning (in red) days over Shanghai. The data for each episode was based on hourly-averaged samples from 7 a.m. to 6 p.m. in every day, 60 × 2 samples in total.

AMTD
6, 11011–11054, 2013

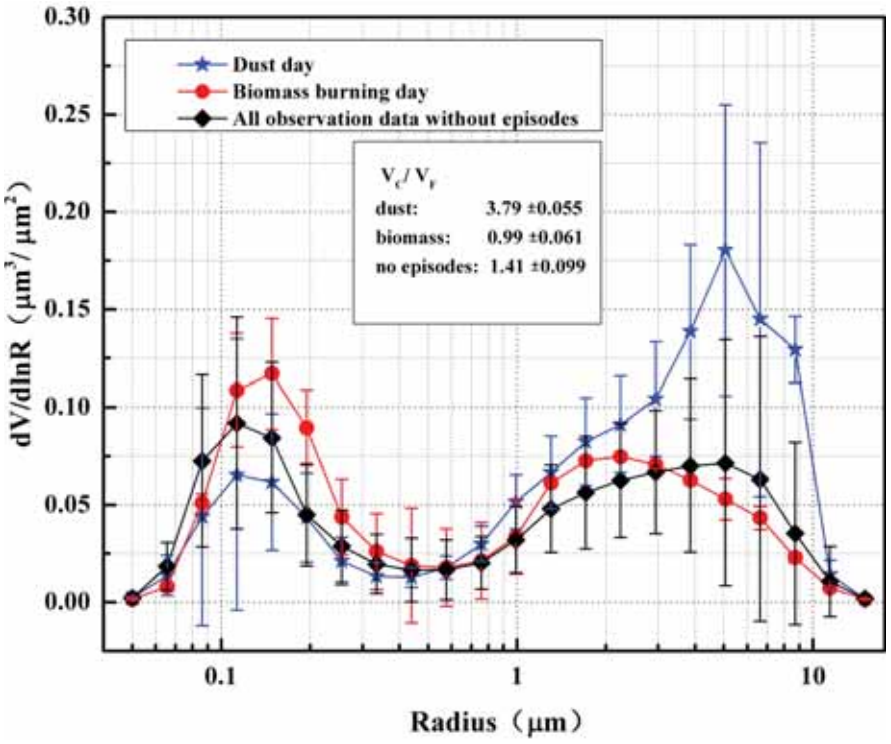

Fig. 7. Average aerosol volume size distribution with standard deviation in the observation period over Shanghai. The averages and deviations were calculated from each inversed volume concentration in 22 radius during five dust days (in blue), five biomass burning days (in red) and forty normal days (in black).

AMTD
6, 11011–11054, 2013

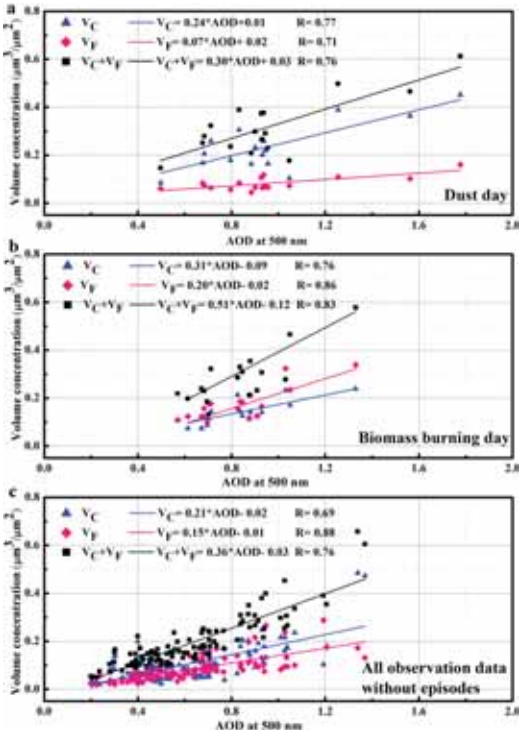

Fig. 8. The scatter-plot of aerosol volume concentration in the accumulation mode and coarse mode with AOD at 500 nm in **(a)** dust days; **(b)** biomass burning days; and **(c)** days without episodes over Shanghai. The blue line is the fitting line of the coarse mode aerosol volume concentration with AOD while the pink line is the fitting line of accumulation mode aerosol volume concentration with AOD, and the black line is the fitting line of the sum of the volume concentration of these two aerosol types with AOD.

AMTD
6, 11011–11054, 2013

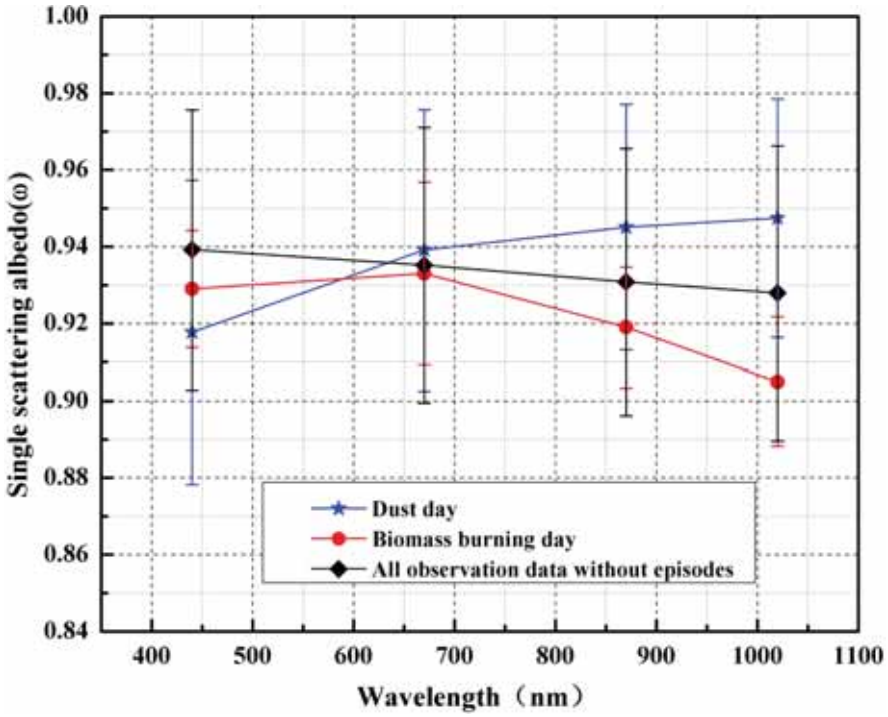

Fig. 9. Average aerosol single scattering albedo at 440, 675, 870 and 1020 nm with standard deviation in the observation period over Shanghai. The averages and deviations were calculated from each inversed SSA during five dust days (in blue), five biomass burning days (in red) and forty normal days (in black).

AMTD
6, 11011–11054, 2013

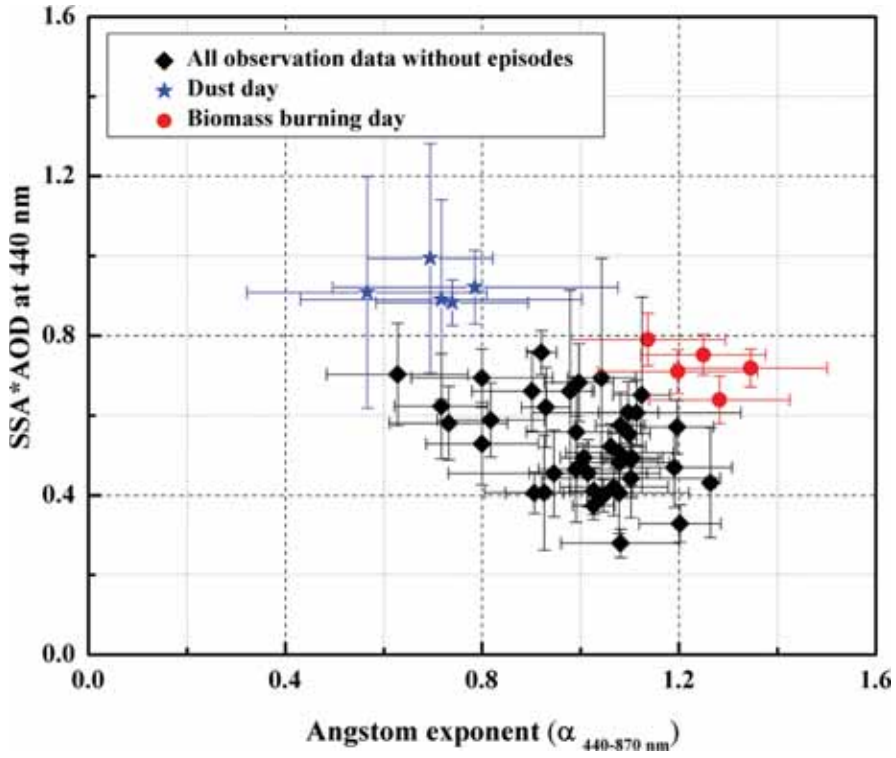

Fig. 10. Scatterplot of daily-averaged Ångström exponent and scattering coefficient (AOD · SSA at 440 nm) in the observation period over Shanghai. The averages with standard deviation were calculated from all inversed AOD, SSA and Ångström exponent in each observation day. Five samples were for dust (in blue) and five samples were for biomass (in red) while forty samples represented normal condition (in black).

AMTD
6, 11011–11054, 2013

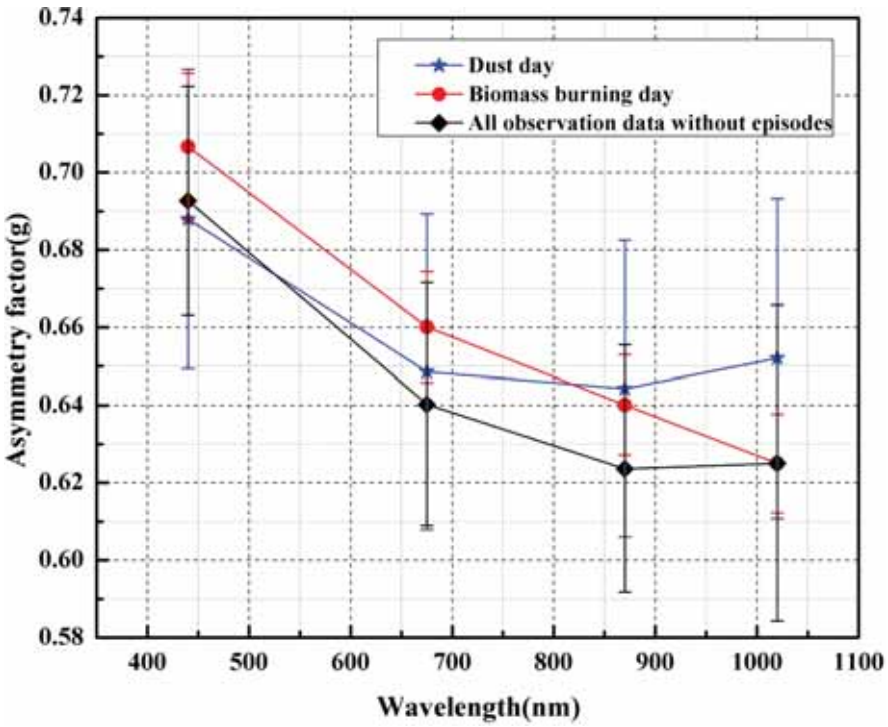

Fig. 11. Average aerosol asymmetry factor at 440, 675, 870 and 1020 nm with standard deviation in the observation period over Shanghai. The averages and deviations were calculated from each inversed ASY during five dust days (in blue), five biomass burning days (in red) and forty normal days (in black).

AMTD
6, 11011–11054, 2013

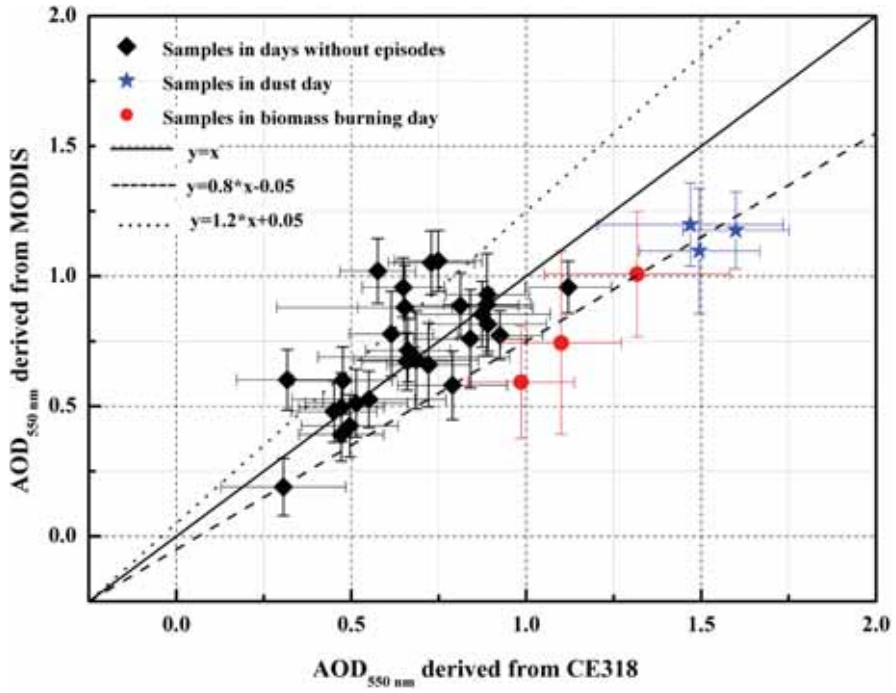

Fig. 12. Scatterplot of daily-averaged AOD at 550 nm derived from MODIS (C051 products) and CE318 in the observation period over Shanghai. There were 41 available samples in total (three for dust and three as biomass samples). The spatial averages with standard deviations of MODIS AOD were calculated in the range of 40 km × 40 km. AOD with its error bars from CE318 were temporal averages within ±30 min when satellite passed and averaged between AOD at 440 and 670 nm.

AMTD
6, 11011–11054, 2013